UKAEA-CCFE-PR(23)152

Peng Shi, Yuhan Wang, Li Gao, Hongjuan Sun, Qinghu Yang, Xin Xu, Chengshuo Shen, Yanqiu Chen, Qinlin Tao, Zhipeng Cheng, Haosheng Wu, Lu Wang, Zhongyong Chen, Nengchao Wang, Zhoujun Yang, Jingchun Li, Yonghua Ding, Yuan Pan, J-TEXT team

Critical roles of edge turbulent transport in the formation of high-field-side high-density front and density limit disruption in J-TEXT tokamak

Critical roles of edge turbulent transport in the formation of high-field-side high-density front and density limit disruption in J-TEXT tokamak

Peng Shi, Yuhan Wang, Li Gao, Hongjuan Sun, Qinghu Yang, Xin Xu, Chengshuo Shen, Yanqiu Chen, Qinlin Tao, Zhipeng Cheng, Haosheng Wu, Lu Wang, Zhongyong Chen, Nengchao Wang, Zhoujun Yang, Jingchun Li, Yonghua Ding, Yuan Pan, J-TEXT team

This is a preprint of a paper submitted for publication in Nuclear Fusion

Critical roles of edge turbulent transport in the formation of high-field-side high-density front and density limit disruption in J-TEXT tokamak

Peng Shi[1,2,3], Yuhan Wang[2] , Li Gao[2]*, Hongjuan Sun[1], Qinghu Yang[2], Xin Xu[2], Chengshuo Shen[2], Yanqiu Chen[2], Qinlin Tao[2], Zhipeng Cheng[2], Haosheng Wu[4], Lu Wang[2], Zhongyong Chen[2], Nengchao Wang[2], Zhoujun Yang[2], Jingchun Li[5], Yonghua Ding[2], Yuan Pan[2] and J-TEXT team

[1]United Kingdom Atomic Energy Authority, Culham Centre for Fusion Energy, Culham Science Centre, Abingdon, Oxon, OX14 3DB, United Kingdom

[2]International Joint Research Laboratory of Magnetic Confinement Fusion and Plasma Physics, State Key Laboratory of Advanced Electromagnetic Engineering and Technology, School of Electrical and Electronic Engineering, Huazhong University of Science and Technology, Wuhan 430074, China

[3]Southwestern Institute of Physics, PO Box 432, Chengdu 610041, People's Republic of China

[4]NEMO Group, Dipartmento Energia, Politecnico di Torino, Corso Duca degli Abruzzi 24, 10129, Torino, Italy

[5]Department of Earth and Space Sciences, Southern University of Science and Technology, Shenzhen 518055, People's Republic of China

*Corresponding author: gaoli@mail.hust.edu.cn

Abstract:

This article presents an in-depth study of the sequence of events leading to density limit disruption in J-TEXT tokamak plasmas, with an emphasis on boudary turbulent transport and the high-field-side high-density (HFSHD) front. These phenomena were extensively investigated by using Langmuir probe and Polarimeter-interferometer diagnostics. The research reveals a consistent pattern of events as the plasma density ramps up: the collapse of the sheared radial electric field, the enhancement of a boundary broadband turbulence ($50\sim80kHz$), the increase of boundary particle transport induced by this turbulence, edge cooling and the emergence of the HFSHD front. These phenomena occur once the plasma density exceeds a critical value. Importantly, by exploring plasmas with varying edge safety factor (q_a), it's revealed that the density thresholds for these phenomena are all inversely proportional to q_a. The findings offer valuable insights into the mechanisms underlying density limit disruptions in tokamak plasmas, suggesting that the enhancement of edge turbulent transport plays crucial roles in the edge cooling and triggering the HFSHD front. For the first time, a strong link between the edge turbulent transport and the HFSHD front has been observed. In addition, the boundary electron temperature consistently drops to the same value in different q_a discharges, which can potentially offer an explanation as to why the density limit appears to be independent on q_a.

1. Introduction

High density is a prerequisite for the operation of future fusion reactors, since the power produced by fusion is proportional to the square of plasma density. To achieve higher economic efficiency in future large tokamaks, a high plasma density is highly desirable for the next-step tokamaks, such as the International Thermonuclear Experimental Reactor (ITER) and Chinese Fusion Engineering Testing Reactor (CFETR) [1-2]. However, experiments in tokamaks show that the plasma operating densities always have an upper limit. At present, the Greenwald density (line-averaged) scaling $n_G[10^{20}m^{-3}] = I_P[MA]/\pi a^2[m^2]$ is empirical for the density limit that is widely applicable to devices such as the Alcator, DIII and PBX [3-4].

Experimental and theoretical studies of the density limit have been pursued for decades, leading to a multitude of explanations for the underlying physical mechanisms. In experiments where the plasma density is increased via continuous gas puffing, various instabilities have been observed as the plasma density gradually ramps up to the density limit disruption. Results across different devices have revealed common characteristics of these physical phenomena during the process of density limit disruption [5-6]. For instance, thermal-radiation instabilities [7-8], edge cooling [5,9], boundary constraint deterioration, and eventual MHD instabilities [10-11] are consistently observed during the process of density ramp-up. The highly reproducible nature of these phenomena and their occurrence at the plasma boundary suggest that the boundary plasma behaviors play an important role in the physical mechanism of density limited disruption [12]. Moreover, it was found that the Greenwald density limit could be exceeded by optimizing fueling techniques, which can increase the central plasma density while maintain the boundary plasma density. This discovery provides strong evidence that the evolution of the boundary parameters plays a crucial role in determing the density limit [13].

Multifaceted Asymmetric Radiation From the Edge (MARFE), one of the most remarkable macro-phenomena observed in the process of density limit disruption, is widely believed to trigger the MHD instability and major disruption. MARFE is characterized by high electron density, low temperature, strong volumetric recombination, and commonly occurs at the high field side (HFS) near the inner wall of the tokamak in limiter [14]. Following the appearance of MARFE, the line integral density at the HFS boundary increases sharply and the radiated power in the MARFE region reaches 30-50% of the total heating power [14-15]. In divertor plasmas, the phenomena tend to manifest close to the X-point region, and often accompanied by divertor detachment, which is referred to as 'X-point MARFE' or 'divertor MARFE' [16-17].

In recent years, a high-field-side high-density (HFSHD) phenomenon has been observed in the high-density operation on both divertor and limiter plasmas. In ASDEX-U and JET divertor plasmas, the HFSHD front appears near the inner target and moves to the X-point as the plasma density increases, followed by the X-point MARFE and divertor detachment [18-22]. In the J-TEXT limiter plasmas, the HFSHD front is found to form at the midplane of HFS edge, and tends to move towards the low field side (LFS) just prior to the density limit disruption [23]. The HFSHD front shares many similarities to MARFE, such as both occurring at the HFS boundaries and exhibiting localized high density. However, there are also distinct differences between the two phenomena. The radiation power from the region of HFSHD front is significantly lower than MARFE. And the HFSHD front is much stable at the inner target or HFS edge across a broad range of plasma density, which is in contrast to the unstable behavior of MARFE. According to the above observations, the author believe that the HFSHD front is an early form of MARFE.

In addition to thermal-radiation instabilities, micro-turbulence instability also plays an important role in boundary cooling and density limit disruption [24-25]. Previous experiments in J-TEXT have observed the collapse of edge flow shear and a decrease of the ratio of Reynolds power to turbulence production during the ramp-up of plasma density [5]. There weve also observations of increased electron particle and heat transport before density limit disruption [26-27]. This findings are consistent with observations on Alcator C-Mod [28] and HL-2A [29]. Furthermore, plasma confinement can be improved by maintaining the edge shear layer and suppressing the boundary particle flux, accomplished by applying a positive bias to [27,30]. This can confirm the roles of edge turbulent transport.

Among those factors potentially contributing to the density limit, multiple factors can interact simultaneously, and the intricate details of their interplay are still open questions. This paper aims to investigate the roles of boundary turbulence in determine density limit and its relationship between with HFSHD. Given that the density threshold of HFSHD front was observed to be closely related to q_a in J-TEXT previous experiments [23], we have conducted a wide study of boundary turbulent transport and HFSHD front across plasmas with various q_a.

The rest of the paper is organized as follows: Section 2 describes the experimental setup and main diagnostics for the investigation of the edge turbulence behaviour and HFSHD front in the J-TEXT tokamak. Section 3 presents the experimental results during the density ramp-up. Section 4 presents conclusion and discussion.

2. Experimental Setup

The J-TEXT tokamak (formerly TEXT-U [31]) is a conventional medium-sized tokamak with a major radius of $R_0 = 1.05\ m$ and minor radius of $a = 0.25 \sim 0.29\ m$. The first wall and the limiter are covered with carbon tiles. In this experiment, we utilized three different positions of limiters - top, bottom and outer (Fig. 1(a)), all located at $r_{Limiter} = 25.5\ cm$. It's noteworthy that there is no limiter at the HFS in our experiments (it was removed recently for the HFS divertor operation), which is quite different to the experiments in our previous publication [23]. The arrangement of the main diagnostics is shown in figure 1. The line-integrated electron density is measured by a multichannel far-infrared laser polarimeter-interferometer system (POLARIS) [32]. This system views the plasma vertically at intervals of $3cm$ in the radial mid-plane, ranging from $r = -24\ cm$ to $r = +24\ cm$, thereby covering the main plasma region ($|r| < 0.94a$), where $r = R - R_0$, as shown in Fig. 1(a) & (b). Here, $r < 0$ and $r > 0$ correspond to the HFS and the low field side (LFS), respectively.

A 36-channel photodiode array (PDA) system is used to measure the line emission of Hydrogen α (H_α) [33]. This system, similar to POLARIS, also covers the HFS and LFS of the tokamak. The sight line of the inner-most three chords go through the area where the HFSHD is located, and only the channels employed in this experiment are showed in Fig. 1(a). The electrostatic probes arrays, also known as the combined Langmuir-magnetic probe (CLMP) [34], are mounted on the window Port#13 at the device's top (Fig. 1(b)). The configuration of the Langmuir probe array is shown in Fig. 1(c). The CLMP consists of eight graphite probes, each with a diameter of 2 mm. Probes 1 - 4 are situated on step 1 with a length of 3 mm, while probes 5 - 8 are on step 2 with the same length. The connecting line of pins 5 and 7 aligns with the direction of the ring, avoiding the shadow effect between the probes. Pins 1 and 3 are distributed along the toroidal direction as a pair of Mach probes. Pins 2 and 4 measure the average floating potential on step1 $V_{f,step1} = (V_{f,2}+V_{f,4})/2$. The pins 6 and 8 spacing $d = 7mm$ are used to measure the average floating potential on step2 $V_{f,step2} = (V_{f,6}+V_{f,8})/2$. Pins 5 and 7 are biased to form a double probe for acquiring the ion saturation current $I_s = (V_{+,5} - V_{-,7})/R_{shunt}$, where R_{shunt} refers to the sample resistor in the double probe circuit. Based on the above configuration, the electron temperature T_e, electron density n_e, the poloidal electric field E_p and the radial electric field E_r can be measured simutaneously by CLMP. Electron temperature is inferred by $T_e = (V_{-,7} - V_{f,step2})/ln2$. Electron density is inferred by $n_e = I_s/(0.49eA_{eff}C_s)$, where e is the elementary charge, C_s is ion sound speed and A_{eff} is the effective current collection area. Plasma potential is inferred by $\varphi_p = V_{f,step2} + 2.5T_e$, and the radial electric field may be inferred from $E_r = -\nabla_r \varphi_p \approx -\nabla_r V_{f,step} - 2.5\nabla_r T_e/e$. When the electron temperature profile does not change significantly, the second term, $-2.5\nabla_r T_e/e$, is negligible. The poloidal electric field is computed as $E_p = (V_{f,6} - V_{f,8})/d$, here, d is the spacing between pins 6 and 8. And the radial electric field E_r can be esitmated by the gradient of floating potential in two steps as $E_r = -\nabla_r \varphi_p \approx -\nabla_r V_{f,step}$. The fluctuations of the parameters are obtained by filtering them with a band-pass FIR digital filter with a bandwidth of $0 - 200\ kHz$ to eliminate high-frequency irregularities that might influence the experimental investigations.

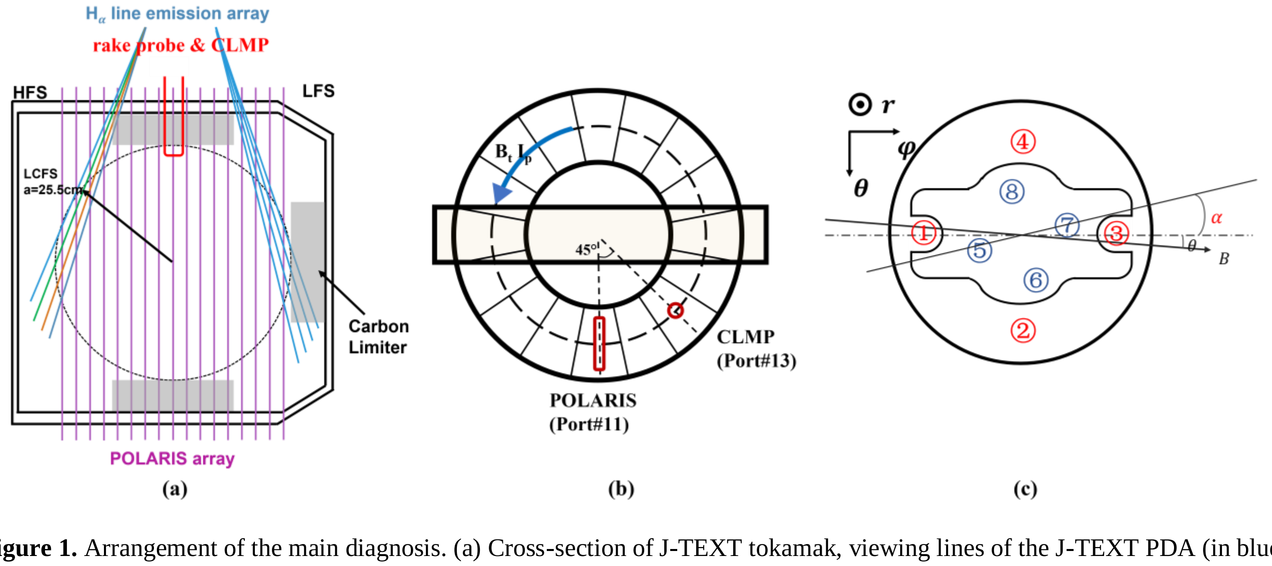

Figure 1. Arrangement of the main diagnosis. (a) Cross-section of J-TEXT tokamak, viewing lines of the J-TEXT PDA (in blue color) and POLARIS (in magenta color), respectively. The CLMP locates at $r = 23.5cm$ and the rake probe array was used for measuring floating potential at $r-a = -3\sim 2\ cm$. (b) Top view of J-TEXT tokamak, POLARIS and CLMP are toroidally separated by 45°. (c) The configuration of CLMP array.

Experimental investigations were undertaken on the J-TEXT tokamak utilizing a limiter configuration in Ohmic hydrogen discharges. Continuous gas puffing was applied throughout the experiments. The ensuing experimental results are based on two distinct discharge conditions, with the corresponding parameters described as follows, unless specailly stated otherwise:

[I] A set of shots with density ramp-up in single shot: plasma current $I_P = 120\ kA$, toroidal magnetic field $B_t = 1.7/2\ T$, safety factor $q_a = 4.4/5$ at the plasma edge, with the central line-averaged electron density ramping up in the range $2{\sim}4.5 \times 10^{19} m^{-3}$, and the Greenwald density limit as $n_G = 5.87 \times 10^{19} m^{-3}$. The CLMP remains fixed at $r = 23.5cm$ in these shots, and a typical plasma traces is shown in Figure 2.

[II] A set of shots with lifting densities shot by shot and constant density in each shot: plasma current $I_P = 120\ kA$, toroidal magnetic field $B_t = 1.7/1.9/2/2.2\ T$, safety factor $q_a = 4.4/4.9/5/5.5$. The central line-averaged electron density hovers around 1.5 to 3$\times 10^{19} m^{-3}$. And the CLMP reciprocates to $r = 23.5cm$ in eash shot, providing the boundary radial profile information under varing electron densities.

For all discharges reported in this paper, the plasma current is sustained as constant, with the boundary safety factor being modified solely by adjusting the toroidal magnetic field.

3. Increase of edge turbulence and transport prior to the onset of HFSHD

Previous experiments have shown that the collapse of edge flow shear is a potential trigger for density limit disruption. Interestingly, this collapse of the edge shear flow precedes the actual disruption considerably. In the J-TEXT, the particular behaviour has been corroborated in the edge region as the line-averaged density approached the density limit. The temporal traces for a typical density ramping discharge are shown in Fig. 2. This discharge has parameters of $I_P = 120\ kA, B_t = 1.7T, q_a = 4.4$. It's notable that the density limit disruption occurs at $t = 600ms$ and the maximum central line-average density is $\bar{n}_{e0} = 4.4 \times 10^{19} m^{-3} = 0.74 n_G$. The central line-averaged electron density keeps ramping up steadily during the constant plasma current ($200ms < t < 600ms$). Fig. 2(e) presents the the density asymmetry between the edge channels of HFS and LFS, signifying the emergence of the HFSHD front at $t = 0.48s$ ($\bar{n}_{e0} = 3.4 \times 10^{19} m^{-3}$).

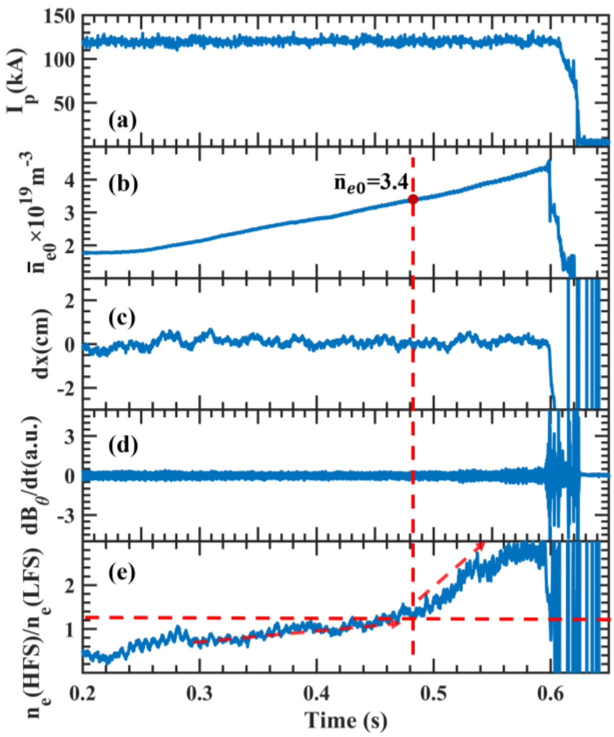

Figure 2. A typical density limit disruption discharge. (a) The total plasma current, (b) central line-averaged density measured by FIR polarimeter–interferometer, (c) the plasma horizontal displacement, (d) the edge magnetic coil signal, and (e) the density asymmetry between the edge channel of HFS and LFS measured by POLARIS.

Furthermore, Fig. 3 (b-d) displays the temporal evolution of the auto-power spectrum pertaining to (b) the floating potential, (c) the ion saturation current, and (d) the poloidal electric field, as measured by CLMP. Meanwhile, Fig. 3(a) presents the temporal evolution of the electron density and edge particle flux.

Insightfully, the auto-power spectrum of the floating potential (Fig. 3(b)) reveals two distinct branches of turbulences, each bearing different characteristic frequencies discernible before $0.4s$. However, the low-frequency ($< 30kHz$) branch of turbulences is unobserved in the auto-power spectrum of ion saturation flow and poloidal electric field, as evidenced in Fig. 3(c) and (d). This implies that the low-frequency turbulence is more indicative of radial electric field fluctuations rather than density fluctuations. Regarding the high-frequency turbulence, it's noteworthy that the characteristic frequency suddenly decreases upon the plasma density exceeding a certain threshold at $0.4s$ (Fig.3(d)), while the amplitude correspondingly increases significantly (Fig.3(c)). Simultaneously, the radial particle flux at the edge experiences a surge of 100% from $0.4s$ to $0.5s$ (Fig.3(a), red lines), while the central line-average electron density merely increases by 10% (Fig. 3(a), blue lines). That clearly indicates that the high-frequency turbulence variations within the high-density region play a crucial role in augmenting particle transport.

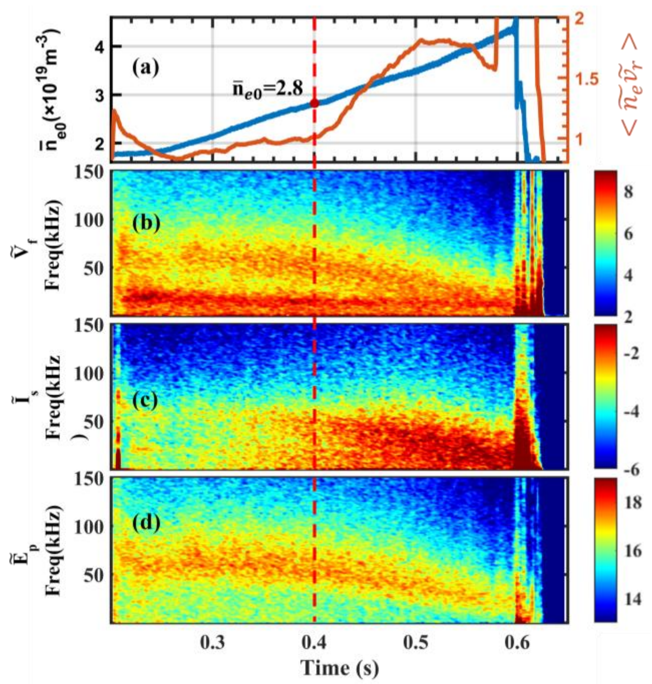

Figure 3. Corresponding to figure 2, the time evolution of (a) central line-averaged density (blue lines) and edge particle flux (red lines), auto-power spectrum of (b) floating potential, (c) ion saturation flow, and (d) poloidal electric field.

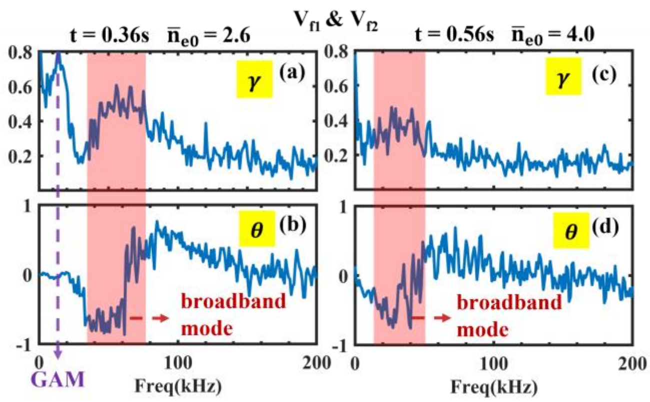

Figure 4. Corresponding to figure 3, (a) & (c) coherence and (b) & (d) phase differencebetween two poloidal separated floating potential $\widetilde{V}_f$, in different central line-averaged density.

In order to further explore the characteristics of these two different turbulences, Fig. 4 presents the correlation and phase difference between the floating potentials ($\widetilde{V}_f$) at two separate poloidal locations. Two cases with different density are compared in Fig. 4. In the case of low density (Fig. 4 (a&b)), the two turbulence branches are markedly distinct. The low-frequency mode exhibits a characteristic frequency of $f \approx 15kHz$, and a characteristic poloidal wavenumber nearing zero, as suggested by the near-zero phase difference (Fig. 4(b)). These features are consistent to the characteristics of geodesic acoustic modes (GAM) [30], which exhibits toroidal and poloidal symmetry with a finite radial wavenumber. The fact that the low-frequency mode cannot be observed on spectra of ion-saturation flow (Fig. 3(c)) and poloidal electrical field (Fig. 3(d)) further substantiates the characteristics of GAM.

Regarding the high-frequency broadband mode, its characteristic frequency remains constant around $60kHz$ in the low density region ($\bar{n}_{e0} < 2.8 \times 10^{19} m^{-3}$), and decreases to $30kHz$ preceding the density limit disruption, as indicated by Fig.4 (c). The phase difference between the two potentials depicted in Fig.4 (b) interestingly shows a shift from negative to positive over the peak frequency of the broadband mode. This implies that the wavelength of the mode is close to the distance of the two distributed potential probes ($d = 7mm$). Therefore, it can be deduced that the poloidal wave number of this broadband mode is approximately $k_\theta = 1/d = 1.4cm^{-1}$. Considering that the edge plasma temperature is around $30eV$(showed in Fig. 8), the normalized wave-number stands at about $\rho k_\theta \approx 0.065$, which falls within the range of Ion Temperature Gradient (ITG)/Trapped Electron Mode (TEM). Additionally, it is worth noting that the GAM-like mode disappears in the high-density plasma as shown in Fig.4 (c). This indicates that the enhancement of I_s fluctuations in high-density plasmas co-occurs with the depression of the GAM-like mode.

Concluding the above experimental observations, after the plasma density surpasses a critical value, several concurrent phenomena are observed at the edge, including the enhancement of broadband turbulence, the suppression of the GAM-like mode, and an increase of radial particle transport. To further study the cause of this turbulent transport augmentation, the auto-power spectrum of the particle flux and E_r profile measured by the CLMP are presented in Fig. 5. From the spectrum of particle flux, it is obvious that the radial particle flux is primarily contributed by the previously discussed broadband turbulence (Fig. 3). Moreover, the low-frequency GAM-like mode almost does not induce any particle transport, which further validates it as a GAM. Therefore, this results suggest that the broadband mode plays a crucial role in boundary transport, and its growth might be related to the suppression of GAM and E_r shear.

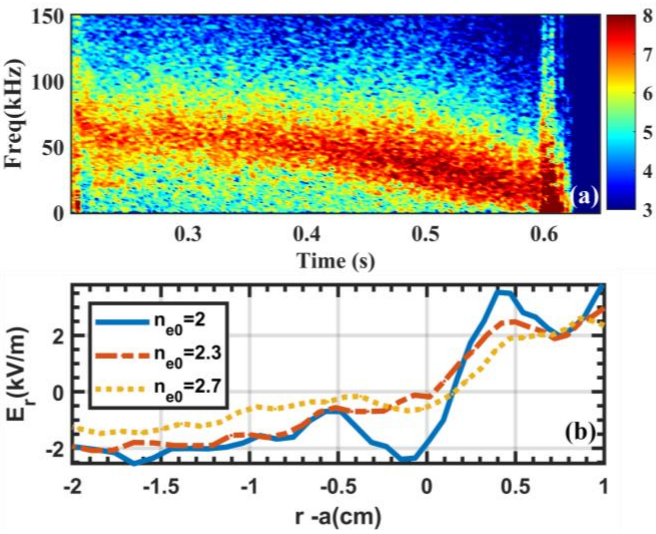

Figure 5. Corresponding to figure 3, (a) auto-power spectrum of edge particle flux Γ. (b) Profiles of edge radial electric field E_r. These profiles are obtained while keeping the plasma density constant. The solid blue, dashed red and dotted yellow lines represent three line-averaged densities $\bar{n}_{e0} = 2, 2.3, 2.7 \times 10^{19} m^{-3}$, respectively.

In order to investigate the E_r profile evolution as plasma density approaches density limit, we have conducted a series of pulses (/#1079986/#1079987/#1079988) with consistent discharge parameters ($I_P = 120kA, B_t = 1.7T$) and incrementally increasing density shot by shot. Then the boundary E_r profile can be obtained by moving the CLMP probe during the flat-top phase of density. As demonstrated in Fig. 5(b), a collapse of the sheared electric field around the last closed flux surface (LCFS) $(r - a = 0)$ is observable as the line-averaged density escalates from 2 to

$2.7 \times 10^{19} m^{-3}$. It's worth noting that the discharge parameters of the three shots in Fig. 5(b) are identical to the shot in Fig. 3. Thus, they should share the same critical density threshold for the enhancement of turbulence and transport. By synthesising the results from Fig. 3 and Fig. 5, we can infer that the collapse of the sheared radial electric field in the edge region is followed by a sudden increase in the intensity of the ion saturation flow perturbation and the edge particle flux.

As illustrated in previous publications [3, 23, 35], the MARFE or HFSHD is the direct cause of MHD instability and major disruption. And the enhancement of turbulence and transport could be responsible for edge cooling and the emergence of MARFE or HFSHD. The rest of this paper will primarily explore the correlation between the turbulent transport and HFSHD. As stated in our previous publication [23], the occurrence of the HFSHD front can be identified by the ratio of the line-averaged density at the edge between HFS and LFS. As demonstrated in Fig. 2(e), when the central line-average density exceeds $\bar{n}_{e0} > 3.4 \times 10^{19} m^{-3}$, the HFS line-average density increases rapidly and the asymmetry develops significantly. This indicates that a local high-density plasma region is formed in the HFS edge as the plasma density exceeds a critical value ($n_{crit} = 3.4 \times 10^{19} m^{-3}$ in this discharge). Such observations are representive of the characteristic features of the HFSHD front phenomenon, as described in [19-20, 23].

To summarize the sequential phenomena as the plasma density approaches to the density limit, a collapse of the sheared electric field is first observed, followed by an abrupt increase in electron density fluctuations and edge particle flux, and later on the HFSHD front appears. Based on the sequence of these events, it can be speculated that the collapse of E_r shear and subsequent increase in turbulent transport is the primary trigger for density limit disruption on tokamaks. Thermal-radiation instabilities like MARFE and HFSHD, as the direct triggers for MHD and major disruption, are simply the outcomes of increased transport. In essence, the density limit is a result of the combined effects of turbulent transport and thermal-radiation instabilities.

4. Effects of edge safety factor on boundary turbulent transport and HFSHD front

To further verify the correlation between the increase in turbulent transport and the onset of the HFSHD front, we investigated the development of the boundary turbulence in plasmas with varied q_a, considering that the critical density threshold of the HFSHD front onset is inversely related to q_a [23].

In Fig. 6, we compare the traces of radial electric field E_r shear rate, edge particle flux and HFS-LFS density asymmetry as a function of line-average density for the shot shown in Fig. 3 (where q_a = 4.4) and another shot with a higher q_a value of 5. The high q_a discharge has parameters: $I_P = 120kA, B_t = 2, q_a = 5$. The maximum central line-average density is $\bar{n}_{e0} = 4 \times 10^{19} m^{-3}$, which equates to $0.68 n_G$. The evolution of particle flux and HFS-LFS density asymmetry are obtained from the discharges with increasing densities in single shot (set [I]), and the E_r shear rate is acquired from the experiments with lifting densities shot by shot (set [II]).

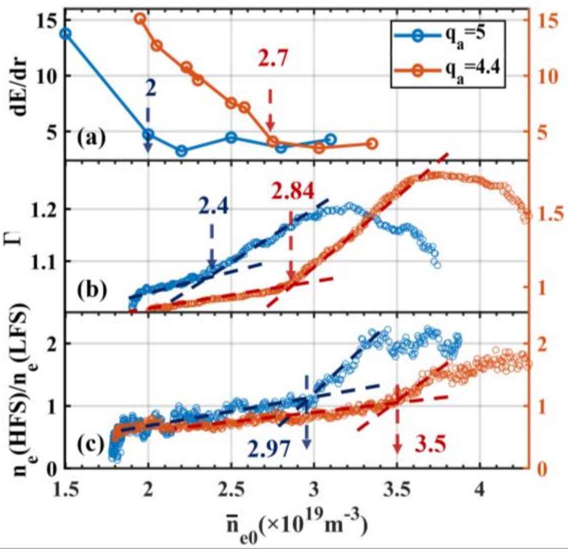

Figure 6. Traces of (a) radial electric field (E_r) shear rate, (b) edge particle flux and (c) HFS-LFS density asymmetry against line-average density for $q_a = 5$ (blue lines) and $q_a = 4.4$ (red lines).

It is noteworthy that both shots undergo a series of events including the collapse of E_r shear, a surge in boundary particle flux, and the emergence of the HFSHD front. And as anticipated, the density threshold for the onset of HFSHD front is significantly lower in the high q_a dsicharge compared to the low q_a one, which has been reported in our previous paper [23]. Interestingly, the critical densities for the collapse of E_r shear and subsequent enhancement of particle transport also demonstrate lower values in the high q_a shot relative to the low q_a shot.

In fact, the findings reported herein can elucidate why the density threshold of HFSHD front is inversely proportional to q_a. As reported in Ref. [23], a critical value of edge collisionality is the trigger for the onset of HFSHD front. The enhancement of edge turbulent transport will accelerate the edge cooling and increases edge collisionality. Therefore, in a high q_a discharge, the lower density threshold of the HFSHD front is a consequence of the lower critical density value associated with the increase in turbulent transport.

The experimental observations detailed above suggest that the edge turbulent transport plays an important role in the emergence of the HFSHD front. At the same time, the HFSHD front also impacts the evolution of boundary parameters. Discharges in the following were conducted with a constant plasma current of $I_P = 120kA$ and a varying toroidal field $B_t = 1.7/1.9/2.2\,T$, in order to scan the safe factor while maintaining the Greenwald density limit. Fig. 7 shows the main traces for the three typical discharges (#1079973 / #1079943 / #1079959) with ramping density in J-TEXT. In these shots, the CLMP was sustained at $r = 23.5cm$, to obtain the evolution of edge parameters along with the density increasing.

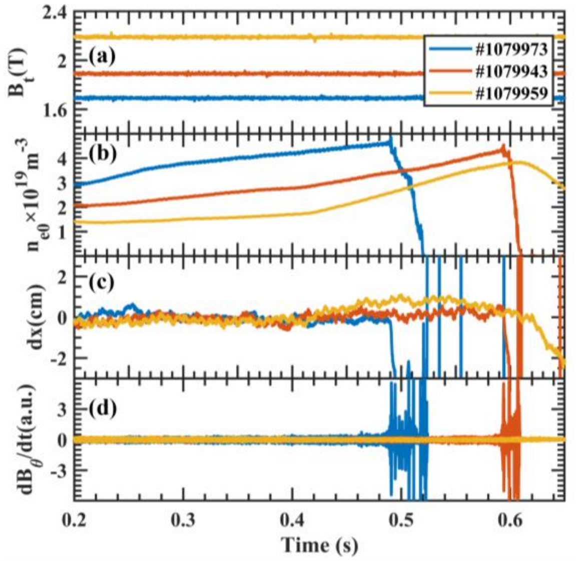

Figure 7. Time evolution of the main parameters for three typical discharges (#1079973/#1079943/#1079959) with ramping density in J-TEXT. (a) toroidal field, (b) central line-average electron density measured by POLARIS, (c) horizontal plasma displacement and (d) the edge Mirnov coil signal.

Corresponding to the three shots in Fig. 7, Fig. 8 shows the HFS-LFS density asymmetry and edge parameters measured by CLMP at $r = 23.5cm$ against the central line-averaged density. The rapid rise in density asymmetry observed in Fig. 8(a) is recognized as a characteristic feature of the emergence of the HFSHD front. Notably, the critical density threshold for the appearance of the HFSHD front appears to be inversely proportional to q_a. These rerults are consistent with the findings in Ref. [23].

Fig. 8 (b) and (c) present the floating potential and electron temperature at $r = 23.5cm$ respectively. Evidently, both of them persistently decrease prior to the appearance of the HFSHD front. To some extent, the evolution of floating potential at $r = 23.5cm$ can represent the trace of E_r shear rate around LCFS, considering that the floating potential is consistenly near to 0 at LCFS ($r = 25.5cm$) in Ohmic plasmas. Consequently, this infers a continuous reduction in the E_r shear rate preceding the onset of the HFSHD front. Importantly, the changes in the boundary E_r

shear rate and T_e with respect to plasma density are notably influenced by the edge safety factor q_a. The decrement of V_f and T_e at the edge is discernibly more premature in low q_a plasmas compared to high q_a discharges. In other words, the values of boundary E_r shear rate and T_e are lower in discharges with a higher q_a, given that the plasma densities are the same.

Subsequent to the emergence of the HFSHD front, both the edge V_f and T_e tend to saturate at certain values. And these critical density thresholds at which saturation occurs are inversely proportional to q_a, which mirrors the behavior of density threshold of the HFSHD front. Interestingly, the final saturation values for both the floating potential and electron temperature appear to be independent of q_a. This implies that the plasma parameters within the radial region affected by HFSHD front are quite stable, regardless of the q_a value. As pointed out in our previous publication [23], the HFSHD front stems from the HFS scrape-off layer (SOL) region, and expands radially and poloidally. A fully developed HFSHD front can extend to a radial location of $r = 20cm$, which is significantly deeper than the location of CLMP ($r = 23.5cm$). As such, the CLMP location is significantly impacted by the HFSHD front once the front is adequately detected by POLARIS. Moreover, according to the one-dimensional flux tube model at the plasma edge (Fig. 7 in Ref. [23]), the LFS end serves as the heat source of the flux tube, under the assumption that the radial heat transport is dominant by the ballooning mode turbulence. Meanwhile, the HFS end, where the cold-dense HD front resides, acts as the heat sink. Therefore, there should have a parallel heat flow from the LFS to HFS end, ensuring the maintenance of thermal equilibrium. The CLMP measures the top of plasma, situated in the middle of the flux tube. The observed results indicate that the plasma parameters in the mid-section of the flux tube where the HFSHD front is located, are stable. This further confirms that the HFSHD front is quite stable in contrast to MARFE. Besides, as shown by Fig. 8(c), the electron temperature in the flux tube affected by HFSHD front appears to stabilize around $\sim 10eV$. This is consistent with the peak of the radiation cooling rate observed for carbon impurity, as discussed in Ref. [36].

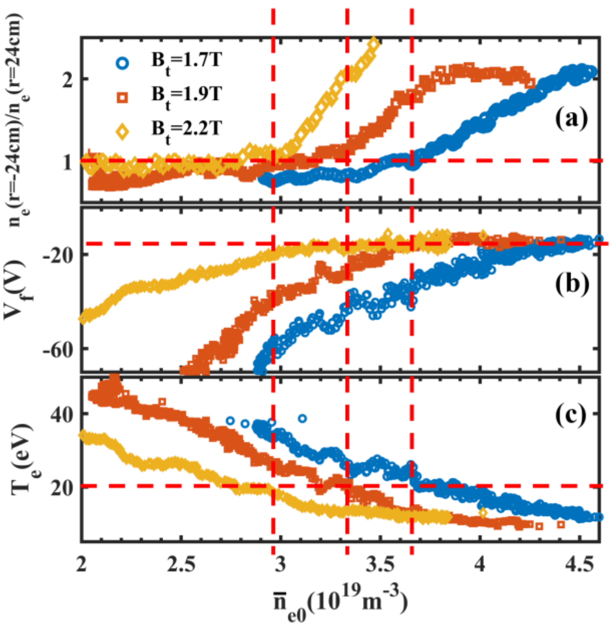

Figure 8. Traces of HFS-LFS density asymmetry measured by POLARIS (a) and edge parameters measured by CLMP against line-average density. (b) Floating potential and (c) electron temperature for different q_a.

In addition, it's worth noting that the HFSHD front consistently occurs when the edge electron temperature drops to around $\sim 20eV$, irrespective of the specific q_a value in the discharge. This suggests that the edge temperature plays a critical role in the formation of HFSHD front. The evolution of edge electron temperature further corroborates the link between the edge turbulent transport and the onset of HFSHD front. The edge temperature is mainly determined by radial transport in Ohmic plasmas, given that the heating source is centralized at the center. The fact that the drop of edge temperature is later in high q_a discharges than the low q_a ones, supports the above hypothesis that enhancement of turbulent transport plays a crucial role in creating the conditions for the HFSHD front occurrence, likely by leading to increased edge cooling and higher collisionality at the plasma edge.

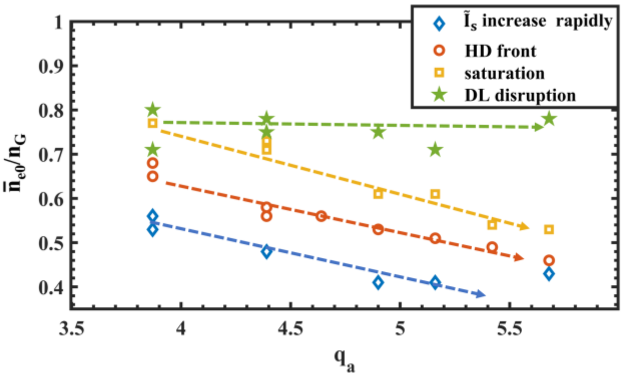

Figure 9. Statistics of density thresholds against safety factor q_a for the rapid increasing of $\tilde{I}_s$ (blue diamond), HFSHD front emergence (red circles), boundary T_e saturation (yellow squares), and the maximum density (green pentagram).

Figure 9 shows the statistics of density thresholds for all the above physical phenomena against boundary safety factor q_a. The series of observations documented provides valuable insights into the sequence of events that occur during plasma density ramp-ups under different q_a in tokamak experiments. The unfolding of events – from the collapse of shear flow, to the swift enhancement of boundary turbulent transport, the emergence of the HFSHD front, the saturation of boundary temperature, and ultimately, the density limit disruption – is strikingly consistent, suggesting a potentially universal mechanism underlying density limit disruption in tokamak plasmas.

Futhermore, the data show that the density thresholds for all the above physical phenomena bear an inverse relationship to q_a. This suggests that higher q_a values prompt the edge cooling and HFSHD front to manifest earlier in the plasma density ramp-up process. Nevertheless, the point of density limit disruption itself doesn't display a significant shift for varying q_a. This could potentially be attributed to the premature onset of edge cooling and HFSHD front, which act as catalysts for density limit disruption, while concurrently, a high q_a works to stabilize MHD instability.

5. Summary and Discussion

In this paper, we report the discovery and analysis of boundary turbulence behaviour and the high-density front as the density approaches density limit on the J-TEXT tokamak. The experiments were carried out by Ohmic heating and the plasma density was increased by continuous gas puffing without the use of auxiliary system or external drives. The following is a summary of the experimental findings:

(a) Two different branches of turbulences are observed by Langmuir probes at $\rho = 0.92a$. The low-frequency ($f \approx 15kHz$) branch of turbulence is identified as Geodesic Acoustic Mode (GAM), characterized by its dominance in potential fluctuations, zero poloidal wavenumber ($k_\theta \approx 0$) and lack of contribution to radial particle transport. The high-frequency ($50\sim80kHz$) turbulence is a broad-band mode that can be identified in the auto-power spectrum of the ion saturation flow and poloidal electric field. The edge particle flux is found to be mainly contributed by the high-frequency trubulence.

(b) After the plasma density exceeds a critical value, there is a sudden amplitude increase in high-frequency turbulence, along with a decrease in its frequency. Concurrently, the GAM is suppressed and the radial particle flux increases. In addition, a collapse of E_r shear around the LCFS is observed at a lower density than threshold for turbulent transport enhancement. Furthermore, the appearance of the HFSHD front follows the increase of boundary turbulence.

(c) The edge floating potential and electron temperature measured by CLMP consistently decrease after the increase of turbulent transport. Interestingly, they appear to stabalize at a certain value after the onset of HFSHD front.

In various q_a discharges, the HFSHD front always accurs when the edge T_e drops to around $\sim 20eV$, even though the density threshold is apparently different.

Based on the above observations, we can outline a series of boundary events leading to density limit disruption. By sequence, they are the collapse of E_r shear, enhancement of turbulent transport, suppression of GAM, T_e decrease and the appearance of HFSHD front. This sequence indicates that the collapse of E_r shear and subsequent enhancement of turbulent tranport is the primary cause for density limit disruption in tokamak. The HFSHD front, which is the direct cause for MHD and major disruption, is just the result of enhancement of turbulent transport.

Importantly, the pattern of sequential events is consistent in various density climbing discharges. And the density thresholds for these phenomena are all inversely proportional to q_a. This results further suggest the crucial roles of edge turbulent transport in density limit disruption. In higher q_a discharge, the edge cooling and HFSHD front have a lower density threshold is because that the collapse of E_r shear and increase of turbulent transport happen earlier in the ramp-up of plasma density. Moreover, the effects of q_a on the density threshold of the collapse of E_r shear can be explained by the theory proposed by Hajjar and Diamond [37]. According to that theory, as the plasma response passes from adiabatic ($\alpha > 1$) to hydrodynamic ($\alpha < 1$), the edge zonal shear layer collapses and turbulence is enhanced. The critical variable α is the adiabaticity parameter, equals to $k_z^2 v_{th}^2/(v_{ei}|\omega|)$. Here, k_z is the parallel wavenumber, can be estimated to be $\sim 1/qR$. Consequently, the α is inversely dependent on q_a, suggesting a lower density threhold for collapse of edge shear layer.

However, the density limit itself exhibits a very weak dependence on q_a. This could potentially be interpreted as the cumulative effects of q_a on micro-turbulence and macro-MHD. On one hand, higher the q_a could lead to a lower the density threshold for the collapse of E_r shear and resultant HFSHD front, which is detrimental to plasma confinement. On the other hand, higher q_a values tend to stabilize the MHD instability. Taken together, from a qualitative point of view, different q_a values do not significantly impact the final value of density limit disruption. It is important to note that the above speculations are qualitative rather than quantitative. We will further conduct simulation studies in the future to demonstrate the feasibility of these speculations.

Acknowledgements: This work is supported by the National MCF Energy R&D Program under Grant No. 2018YFE0310300 and the National Natural Science Foundation of China under Grant No. 11905080 and 51821005. This work has been also part-funded by the EPSRC Energy Programme [grant number EP/W006839/1]

References:

[1] Shimada M *et al* 2007 *Nuclear Fusion* **47** S1-S17

[2] Wan Y *et al* 2017 *Nuclear fusion* **57** 102009

[3] Greenwald M *et al* 1988 *Nuclear fusion* **28** 2199-2207

[4] Allen J M *et al* 1986 *Plasma physics and controlled fusion* **28** 101-112

[5] Ke R *et al* 2022 *Nuclear fusion* **62** 76014

[6] Schuller F C 1995 *Plasma Phys. Control. Fusion* **37** A135

[7] Fielding S J *et al* 1977 *Nuclear fusion* **17** 1382-1385

[8] Zanca P *et al* 2019 *Nuclear fusion* **59** 126011

[9] Hajjar R J *et al* 2018 *Physics of Plasmas* 2018 **25** 062306

[10] Allen J M *et al* 1986 *Plasma physics and controlled fusion* **28** 101-112

[11] Lipschultz B *et al* 1984 *Nuclear fusion* **24** 977-988

[12] Zanca P *et al* 2017 *Nuclear fusion* **57** 56010

[13] Brower D L *et al* 1989 *Nuclear fusion* **29** 1247-1254

[14] Lipschultz B *et al* 1998 *Physical review letters* **81** 1007-1010

[15] Stabler A *et al* 1992 *Nuclear fusion* **32** 1557-1583

[16] Maingi R *et al* 1999 *Journal of Nuclear Materials* **266-9** 598-603

[17] McCracken G M *et al* 1987 *Journal of Nuclear Materials* **145** 181-185

[18] Potzel S *et al* 2013 *Nuclear fusion* **54** 13001-19

[19] Manz P *et al* 2017 *Nuclear Materials and Energy* **12** 1152-1156

[20] Reimold F *et al* 2017 *Nuclear Materials and Energy* **12** 193-199

[21] Reimold F *et al* 2015 *Journal of Nuclear Materials* **463** 128-134

[22] Potzel S *et al* 2015 *Journal of Nuclear Materials* **463** 541-545

[23] Shi P *et al* 2021 *Plasma physics and controlled fusion* **63** 125010

[24] Brower D L *et al* 1991 *Physical review letters* **67** 200-3

[25] Rapp J *et al* 1999 *Nuclear fusion* **39** 765-776

[26] Long T *et al* 2021 *Nuclear fusion* **61** 126066

[27] Ke R *et al* 2022 *Nuclear fusion* **62** 76014

[28] LaBombard B *et al* 2001 *Physics of Plasmas* **8** 2107-2117

[29] Hong R *et al* 2018 *Nuclear Fusion* **58** 016041

[30] Sun Y *et al* 2014 *Plasma physics and controlled fusion* **56** 015001

[31] Zhuang G *et al* 2011 *Nuclear fusion* **51** 094020-11

[32] Wang Y H *et al* 2022 *Plasma Science and Technology* **24** 064001

[33] Zhang X L *et al* 2014 *Review of Scientific Instruments* **85** 11E420

[34] Yang Q *et al* 2022 *Plasma science & technology* **24** 54005

[35] Shi P *et al* 2017 *Nuclear fusion* **57** 116052

[36] Neuhauser J *et al* 1986 *Nuclear fusion* **26** 1679

[37] Hajjar R J *et al* 2018 *Physics of Plasmas* **25** 062306